NANO LETTERS

pubs.acs.org/NanoLett

Letter

Nanoscale Mapping of Morphology of Organic Thin Films

Jongchan Kim, Shaocong Hou, Haonan Zhao, and Stephen R. Forrest*

Cite This: *Nano Lett.* 2020, 20, 8290–8297

Read Online

ACCESS | Metrics & More | Article Recommendations | Supporting Information

ABSTRACT: We determine precise nanoscale information about the morphologies of several organic thin film structures using Fourier plane imaging microscopy (FIM). We used FIM microscopy to detect the orientation of molecular transition dipole moments from an extremely low density of luminescent dye molecules, which we call "morphology sensors". The orientation of the sensor molecules is driven by the local film structure and thus can be used to determine details of the host morphology without influencing it. We use symmetric planar phosphorescent dye molecules as the sensors that are deposited into the bulk of organic film hosts during the growth. We demonstrate morphological mapping with a depth resolution to a few Ångstroms that is limited by the ability to determine thickness during deposition, along with an in-plane resolution limited by optical diffraction. Furthermore, we monitor morphological changes arising from thermal annealing of metastable organic films that are commonly employed in photonic devices.

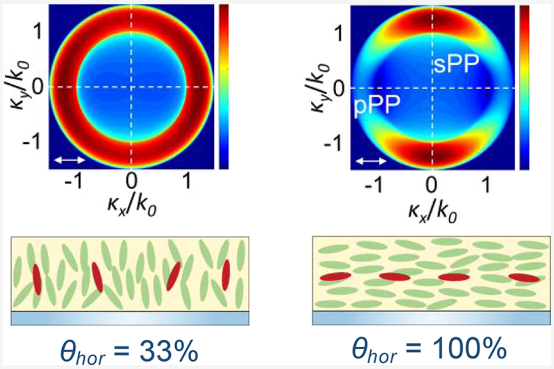

KEYWORDS: *van der Waals solid, nanoscale, morphology, organic, microscopy, dipole orientation*

1. INTRODUCTION

Understanding morphology is fundamental to revealing the structure−property relationships of solids.[1,2] Disordered materials are of particular interest because their morphology is rarely in the lowest-energy equilibrium state and hence can be complex and metastable or even unstable over time.[3,4] Organic molecular solids, which are the foundation of a large range of devices such as organic light-emitting devices and organic photovoltaics, are particularly important members of the class of disordered materials as they are bonded by relatively weak van der Waals (vdW) forces.[5] For this reason, considerable work has been done to develop methods for revealing their morphologies, including reciprocal and real space measurements from X-ray,[6] electron and light sources,[7−9] and scanning probe microscopies.[10,11] Unfortunately, the access to detailed bulk or interface structures using these techniques has been limited by the spatially averaged information on the bulk, the potential damage that they inflict on the sample due to physical contact or by high energy probe beams,[12] their difficulty of use and complexities in data analysis, or their shallow probing depth.

In this work, we reveal the detailed nanoscale morphology within archetype organic electronic thin films using Fourier plane imaging microscopy (FIM), which is a class of fluorescence microscopy that has been used for detecting emissive transition dipole orientations in various materials.[13−23] Advantages of fluorescence microscopy arise from a wide selection of dye molecules available for tagging the structural elements, highly sensitive and position-dependent measurement, and the opportunity to monitor dynamic processes in real time. With an appropriate selection of dye molecules and analysis techniques, determining the local film morphology is possible. By depositing phosphorescent dye molecules at strategic positions within a host organic thin film, their luminescence provides high resolution, depth and area-dependent structural maps of the host. The FIM-plus-dye molecule combination is used to create 3D morphological maps of changes arising from thermal annealing in a stacked bilayer film, and at the interfaces. The volume resolution of the measurements is at the Ångstrom scale in the direction normal to the film plane that is limited only by the flatness of the predeposited film and the ability to accurately determine layer thickness during deposition, and has a resolution of approximately half the visible wavelength (~200 nm) within the plane.

2. RESULTS

Morphology measurements comprise two parts, dye sensor layer placement followed by polarization and spatially sensitive optical observation of the dye emission pattern. We start by

Received: August 27, 2020
Revised: October 28, 2020
Published: November 2, 2020

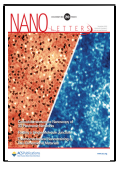

https://dx.doi.org/10.1021/acs.nanolett.0c03440
Nano Lett. 2020, 20, 8290–8297

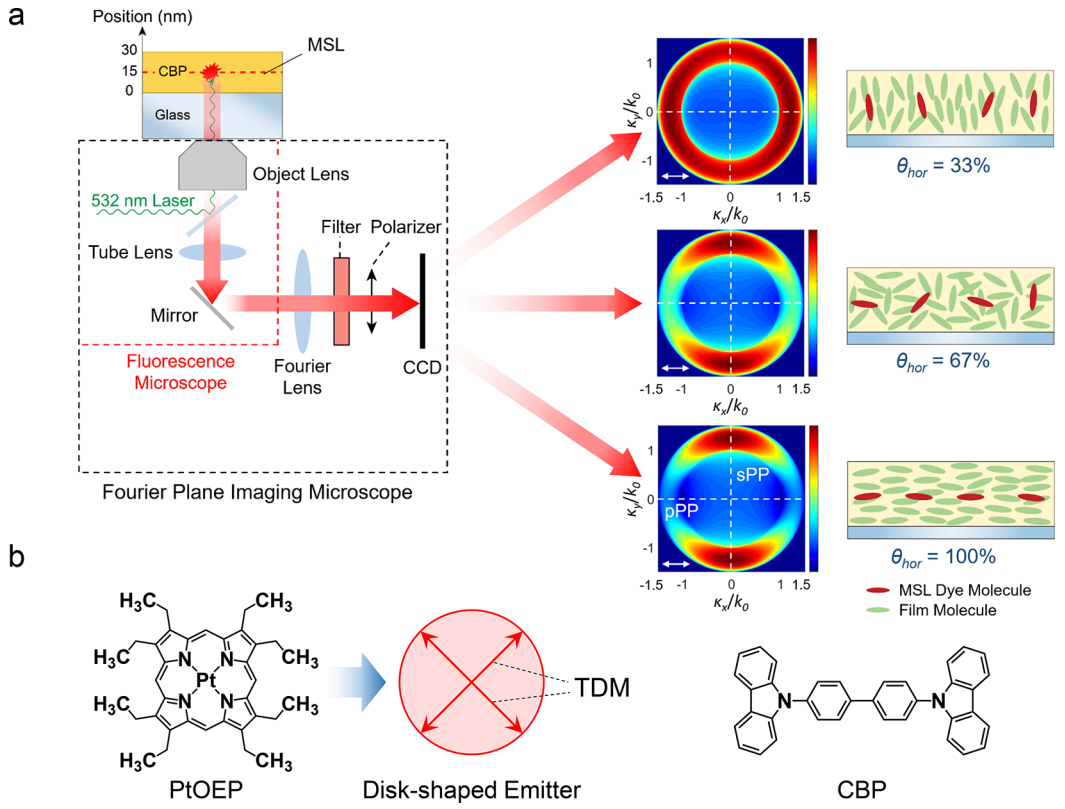

Figure 1. Morphological sensing layer concept. (a) Red dashed line box shows a schematic of the fluorescence microscope, and the black box shows the imaging system. Polar images (center) at different polarizations (shown by arrows) corresponding to the emission due to orientation of the dye molecules in the MSL (red ovals, illustration to right) in the morphology of the host matrix (green ovals). (b) Molecular structural formulas of PtOEP and CBP. Because of its square planar D_{4h} symmetry, PtOEP has two orthogonal transition dipole moments (TDMs).

depositing a submonolayer (<1 Å) of dye molecules, called morphological sensing layers (MSLs), at a desired position in the film under test, as illustrated in Figure 1a and the Methods section (in Supporting Information). With an appropriate selection of dye molecule, the orientation of the transition dipole moments (TDMs) of the population is correlated with its environment, thus revealing the morphology at the deposited position.[24] In this work, red-emitting octaethylporphyrin-Pt (III) (PtOEP) is used for the sensor molecule. This is a square, dihedral Pt-complex with a 4-fold symmetry (D_{4h} symmetry). We use the technologically significant CBP (4,4′-Bis(N-carbazolyl)-1,1′-biphenyl) as the material under study because of its well-known structure, film-forming properties, and low glass-transition temperature (T_g), which enables a facile change of morphology via thermal annealing.[2,25]

The MSL orientation is determined using FIM images that are highly sensitive to the orientation of the radiative TDM relative to the substrate plane.[13,14] The optical pump of the fluorescence microscope locally excites the MSL, as shown in Figure 1a, and the photoluminescence of the dye molecules is incident on a CCD array through the objective lens. A linear polarizer (whose directions are indicated by arrows in the bottom-left corners of the simulated polar plots in the right panel) is used to separate the emission in the two orthogonal planes, corresponding to p-polarized (pPP) and s-polarized (sPP) planes. The FIM experimental configuration is shown in Supporting Information, and Figure 1a. The orientation of the dye molecules is determined by comparing the obtained polar plot with a simulation based on a dipole model using dyadic Green's function analysis[23] (see Methods). We define θ_{hor} as the ratio of the intensity of emission of horizontally aligned (relative to the substrate plane) to the total number of TDMs in the film. Then θ_{hor} = 100% for all TDMs oriented parallel to the substrate (in the *x, y* plane), θ_{hor} = 67% for random and 0% for complete vertical (*z*) alignment. In the right panel of Figure 1a, we show simulated plots of the photoluminescence intensity at different angles (known as polar plots) corresponding to θ_{hor} from 33 to 100%. A detailed interpretation of polar plot results is provided in the Figure S1.

PtOEP is a disk-shaped molecule comprising two orthogonal TDMs in the molecular plane, as shown in Figure 1b.[24] Therefore, 50% of the emission from a perfectly vertically oriented PtOEP molecule is from the horizontally aligned TDM, leading to θ_{hor} between 50 and 100%, otherwise θ_{hor} = 67% for isotropic (i.e., random) molecular orientation. This misrepresents the alignment of PtOEP when compared with a less symmetric molecule that has a single, average TDM with θ_{hor} ranging from 0 to 100%. For this reason, we remove the contribution from one of the two orthogonal TDMs in the PtOEP molecular plane by converting the θ_{hor} of PtOEP molecules using the transform shown in Figure S2. The transformed value is denoted $\theta_{h\text{-}conv}$.

Figure 2a shows the measured orientation from two samples; one with the MSL deposited in the center of a 30 nm thick CBP film, and the other with CBP uniformly doped with 10 vol % PtOEP. Both samples indicate a random orientation as found previously.[2,24,25] The negligible difference between the two samples shows that the MSL precisely and locally represents the amorphous morphology of the bulk film. We then annealed the CBP film at 95 °C, above its T_g (62 °C)[25]

https://dx.doi.org/10.1021/acs.nanolett.0c03440
Nano Lett. 2020, 20, 8290−8297

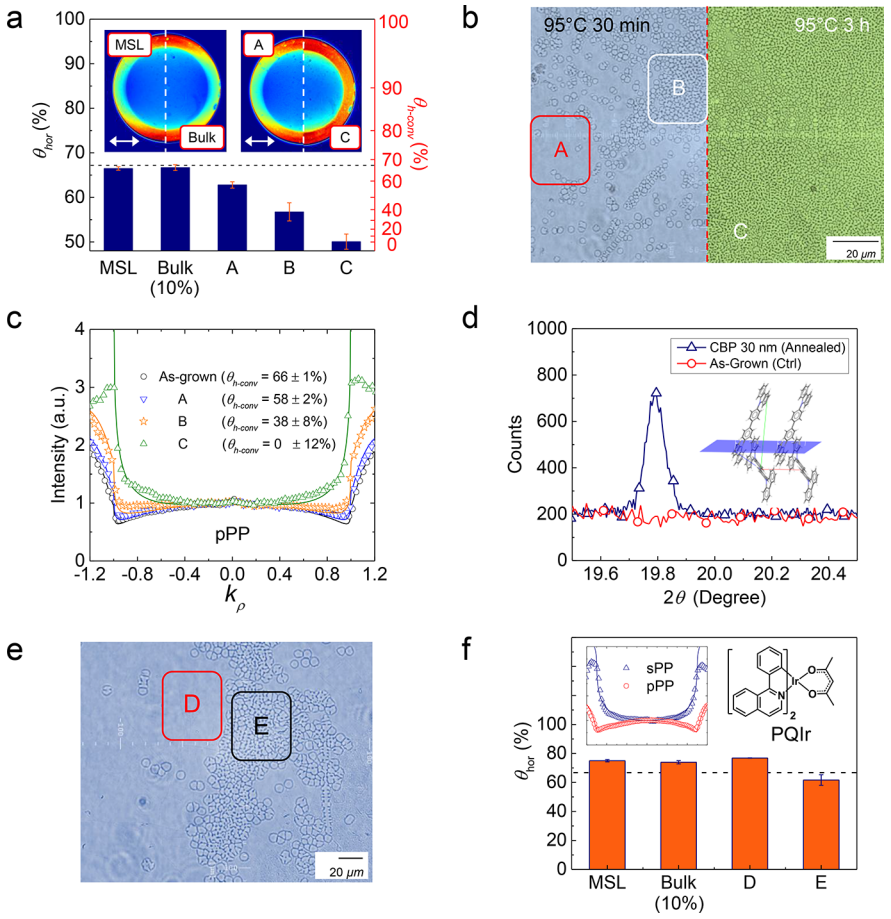

Figure 2. Morphology investigation of a 30 nm thick CBP film. a. Measured θ_{hor} ($\theta_{h\text{-}conv}$) from the CBP film comprising a submonolayer PtOEP MSL in its center, and 10 vol % PtOEP uniformly doped throughout the bulk film. The θ_{hor} ($\theta_{h\text{-}conv}$) from the annealed MSL sample in regions A, B and C are shown in the histogram, where the horizontal dashed line indicates isotropic, random alignment (θ_{hor} = $\theta_{h\text{-}conv}$ = 0.67). The polar plots from each sample are shown at top, with arrows indicating the polarizer direction. (b) Optical micrograph of the 30 nm thick CBP film comprising a PtOEP MSL in its center (15 nm from the substrate) annealed at 95 °C for 30 min (left) and 3 h (right). Colors of the micrographs are added after the measurement for clarity. (c) pPP intensity profile of the as-grown sample, and after annealing in regions A−C. Data are shown by points, and fits are indicated by lines (see Methods). (d) XRD pattern of a 30 nm thick CBP film on a sapphire substrate before and after annealing. Inset: CBP crystal structure with its (031) plane (blue) oriented parallel to the substrate. (e) Optical micrograph of the CBP film with PQIr as the MSL, annealed at 95 °C for 3 h. (f) Measured θ_{hor} ($\theta_{h\text{-}conv}$) of as-grown, 30 nm thick CBP films comprising a PQIr MSL placed in the film center (MSL), PQIr uniformly doped throughout the bulk at 10 vol % (Bulk 10%), and the annealed MSL sample in regions D and E. Inset: Measured p-polarized (pPP) and s-polarized (sPP) planes intensity profiles (data points) along with simulated fits (solid lines) from the as-grown MSL sample. The vertical axis shows the intensity, and the horizontal axis shows the normalized in-plane wave vector (k_ρ). Molecular formula of PQIr is shown on the right.

for 30 min, resulting in no visible change in some regions (A) in the optical micrograph in Figure 2b, whereas there is evidence of crystallization in regions B. After 3 h, the film becomes uniformly crystallized (image C). Figure 2c shows the measured intensity profiles (data points) along with the simulation fits (solid lines) in pPP, normalized to values at k_ρ = 0 in regions A, B, and C. Here, k_ρ is the normalized in-plane wavevector. The fits indicate that $\theta_{h\text{-}conv}$ decreases with annealing from 66 ± 1% to 0 ± 12%, corresponding to a shift from random to principally vertical orientation. X-ray diffraction (XRD) patterns in the Bragg−Brentano geometry of a 30 nm thick neat CBP film are provided in Figure 2d. These data reveal the cause of the decrease in $\theta_{h\text{-}conv}$ in the annealed CBP film. The amorphous, as-deposited film lacks X-ray peaks, whereas after annealing, the film shows a distinct (031) peak corresponding to vertical alignment of the CBP molecules.[26] This is illustrated in the inset showing the orientation of the (031) plane in blue relative to the molecules. In this case, the substrate plane is parallel to (031). We conclude that the reduced $\theta_{h\text{-}conv}$ of the PtOEP MSL is a result of changes in morphology of the CBP film.

The same annealing procedure is followed by using the red-emitting sensor molecule, bis(2-phenylquinolyl-N,C$^{2'}$)-acetylacetonate Iridium(III) (PQIr). This pseudo-octahedral molecule features a bulky, tridentate structure. As before, the sample comprises an ∼1 Å thick sensor layer deposited in the middle of a 30 nm thick CBP film. The as-grown sample shows a primarily horizontal sensor orientation (θ_{hor} = 75 ± 1%). Unlike PtOEP, the complete crystallization of CBP does not occur in the presence of PQIr, even after several hours of annealing, as shown in Figure 2e. Amorphous regions (D) do not show any change of TDM orientation. Indeed, PQIr molecular orientations are randomized even in the crystallized region (E), with significantly lower signal intensity than the as-grown sample. The measured θ_{hor} values from all samples are

https://dx.doi.org/10.1021/acs.nanolett.0c03440
Nano Lett. 2020, 20, 8290−8297

summarized in Figure 2f, showing that PQIr does not clearly describe the structure of CBP, in contrast to PtOEP.

We extended the measurement into the vertical (z) axis to obtain depth-related morphological data. Five samples are prepared comprising a planar heterojunction bilayer of 30 nm 2,2′,2″-(1,3,5-benzinetriyl)-tris(1-phenyl-1-H-benzimidazole) (TPBi) and 30 nm CBP, with PtOEP sensing layers placed in different positions in each of the various samples, labeled P1−P5 in Figure 3a. All films are annealed at 95 °C for 3 h. The

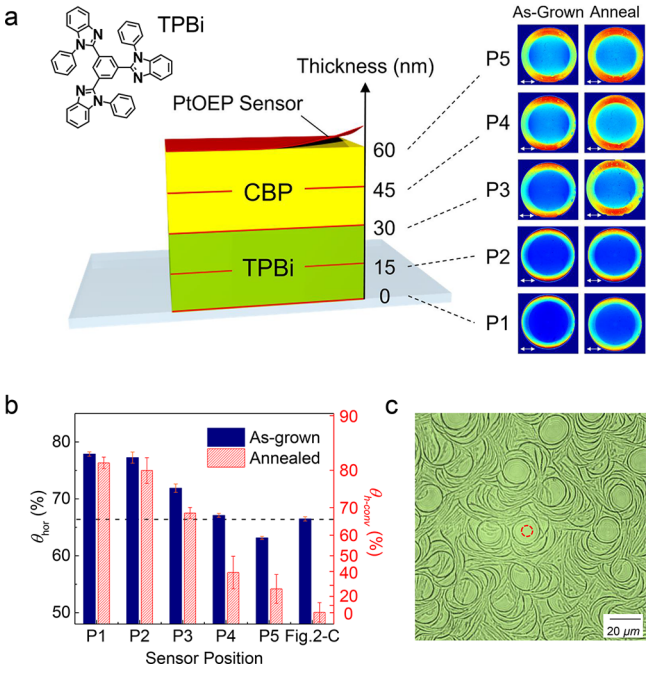

Figure 3. Imaging the morphology of a bilayer thin film. (a) Illustration showing the placement of the PtOEP MSLs within a CBP/TPBi bilayer, with the measured polar plots before and after annealing at the right. Molecular formula of TPBi is shown. (b) Measured θ_{hor} ($\theta_{h\text{-}conv}$) of the as-grown samples, and after annealing for 3 h. The dashed line indicates isotropic alignment. (c) Optical micrograph of the annealed sample. The red circle indicates the area excited by the laser.

polar plots in Figure 3a show a small change in P1−P2 before and after annealing. This contrasts with significant differences observed in positions P4−P5. Measurements of $\theta_{h\text{-}conv}$ for each film are provided in Figure 3b. Figure 3c shows an optical micrograph of the film after annealing, with the red circle showing the optically pumped region in the experiment. The patterns in the micrograph indicate local crystallization of CBP. The $\theta_{h\text{-}conv}$ is reduced by annealing to less than half of its original value in positions P4−P5, while it remains almost constant in P1−P2 in TPBi[25] due to its T_g = 122 °C, which is higher than the annealing temperature. However, the decrease in P4−P5 is still less than in Figure 2b, region C, in the neat CBP film. This suggests that the morphologically stable TPBi film partially "pins" the CBP structure due to contact at the heterointerface, similar to that found for metastable organic mixtures stabilized by including small concentrations of dopant molecules (e.g., PQIr),[27] or by the attachment of a metal cap.[28]

Annealed CBP on a glass substrate in Figure 2 forms a randomly oriented powder in the substrate plane. In contrast, the annealed CBP on TPBi forms spherulites of radially propagating polycrystals. Spherulites appear during diffusion-limited growth,[29] which is caused by the underlying TPBi layer impeding the movement of CBP molecules. In Figure 4a, we used FIM to map morphological variations of sample P5, by moving the beam radially away from the spherulitic region, with a 10 μm interval between each measurement. The orientation of the MSL gradually changes from vertical to random orientation and stabilizes at a 40 μm distance from the spherulite periphery, as shown in Figure 4b. The solid line shows the linear regression of the variation near the spherulitic region, whereas the dashed line shows the average $\theta_{h\text{-}conv}$ in the region of constant morphology.

We also investigated one of the polycrystalline fibers within a spherulite in sample P4 in detail (see image, Figure 4c). The substrate mode intensity shows peaks in the direction parallel to the crystal branch direction, as shown in Figure 4d and Figure S3. The orientational conformation for this phenomenon is illustrated in Figure 4e. Because of its disklike structure, PtOEP emits the majority of its power perpendicular to the molecular plane, causing the vertically aligned PtOEP molecules to show peaks at high-k (corresponding to substrate modes). Also, the peak positions that are parallel to the fibers indicate that the molecular plane aligns perpendicular to the microfiber axis. These data reconfirm that PtOEP follows the CBP host matrix, giving information about the $\pi-\pi$ stacking direction of CBP after annealing.

3. DISCUSSION

Crystallization features witnessed by PtOEP occur after only a 30 min anneal at 95 °C (Figure 2b). The energy provided by annealing at $T > T_g$ = 62 °C of CBP[25] liberates the molecules to form crystallites. In region A, a slight decrease (∼10%) of $\theta_{h\text{-}conv}$ is observed because of morphological changes so small that they do not appear in the micrograph, showing the sensitivity of the method. The crystallization of CBP molecules is visible in region B, corresponding to an additional decrease in $\theta_{h\text{-}conv}$. After 150 min, uniform crystallization spreads across the entire film (region C). The difference in the film appearance between regions B and C is not conspicuous, however, $\theta_{h\text{-}conv}$ decreases after 3 h of annealing, demonstrating continued morphological changes with time. The (031) plane observed via XRD in Figure 2d shows that the CBP molecules in the crystallites formed by annealing are vertically oriented with their c_2 axis tilted approximately 9−17° from the substrate normal. This corresponds to $\theta_{h\text{-}conv}$ = 9−28%, similar to the decrease in Figure 2c. Thus, the decrease in $\theta_{h\text{-}conv}$ measured for PtOEP accurately represents the change in CBP film morphology. Similarly, in Figure 4c, d, the in-plane orientation of PtOEP corresponds to the direction of spherulite growth, as illustrated in Figure 4e.

The measurement precision is, in part, determined by the choice of sensor molecule. This is illustrated by comparing the results in Figure 2 for PtOEP and PQIr, respectively. Compared to planar PtOEP, pseudo-octahedral Ir complexes show less orientation dependence on the host matrix because of the small π-interactions arising from steric hindrance of their bulky molecular structures with the surrounding environment.[25,30] Furthermore, the orientation of heteroleptic Ir complexes with an aliphatic ligand as in PQIr introduce anisotropic interactions, leading to anisotropic orientations with the organic surface during deposition, regardless of the host matrix composition.[31] This can cause a misrepresentation of the host morphology. Furthermore, steric hindrance can impede the ability of the molecules to follow the host

https://dx.doi.org/10.1021/acs.nanolett.0c03440
Nano Lett. 2020, 20, 8290−8297

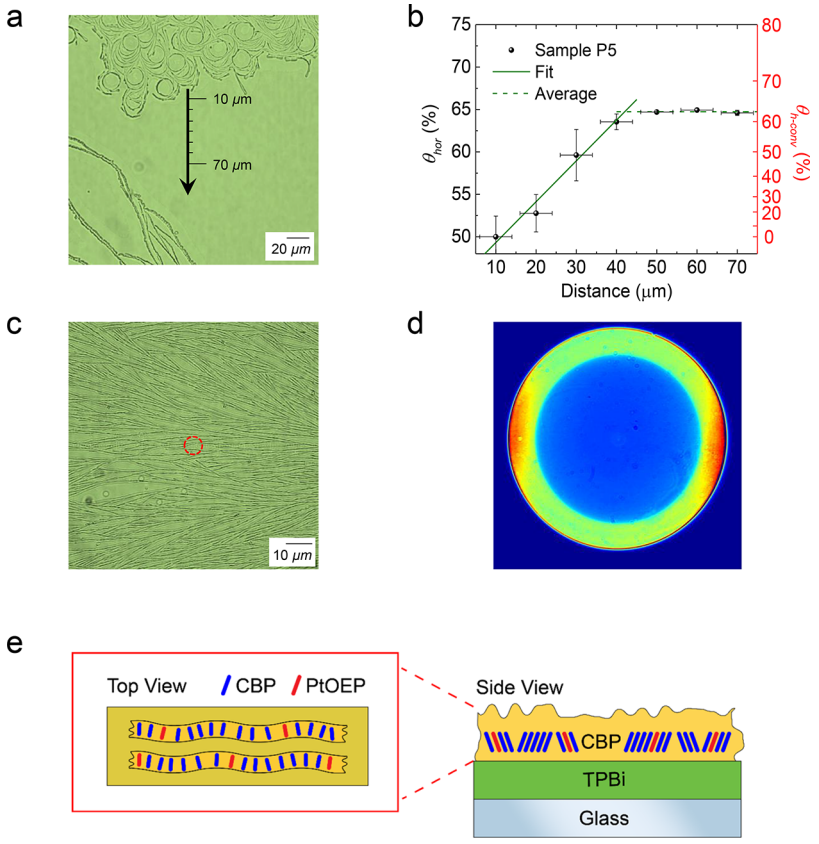

Figure 4. Mapping of the structure of a crystalline grain. (a) Optical micrograph at the periphery of a spherulite in sample P5 after annealing. The arrow shows the line-scan path with measurements made at 10 μm intervals. (b) Measured θ_{hor} ($\theta_{h\text{-}conv}$) following the scanning path in a. The solid line shows a linear regression fit to the data vs distance from the spherulite, until the structure stabilizes close to a random orientation at distances >40 μm (dashed line). (c) Optical micrograph of a polycrystalline fiber of a spherulite in sample P4 after annealing. The red circle indicates the laser excitation area. (d) Polar plot from the red-circled region in c using FIM with the linear polarizer removed. (e) Schematic illustration of the configuration of the PtOEP sensor molecules within the CBP polycrystalline fibers.

morphology, and can even interfere with the progress of crystallization of the host. This is shown by the micrograph in Figure 2e, where only local CBP crystallization occurs, even after hours of annealing above T_g. Amorphous regions (D) show no change in θ_{hor} after annealing as shown in Figure 2f, demonstrating morphological pinning by the PQIr sensors. Indeed, crystallization only takes place when phase separation of CBP and PQIr molecules occurs, as in region E. This, in turn, significantly decreases the PQIr emission intensity because of concentration quenching in sensor aggregates, and randomizes their orientation due to the elevated entropy of PQIr molecules.[32] In conclusion, bulky sensors not only misrepresent the morphology of the surrounding environment, but can also impede the host matrix from achieving its equilibrium structure as in region D in Figure 2e. Hence, planar molecules are better suited for use in 3D FIM + MSL imaging, whereas doping sterically bulky molecules may improve morphological stability of the host even when used in submonolayer quantities. Indeed, FIM in this case has proven to be a useful tool in selecting molecules, while determining their efficacy in stabilizing thin film morphologies.

This leads us to identify the following properties of an appropriate morphological sensor molecule. It should (i) be intensely emissive at wavelengths distinct from that of the host, (ii) have a uniquely defined TDM axis relative to the molecular plane, (iii) be planar to avoid interfering with the morphological development of the host solid, and (iv) be symmetric to prevent the sensor orientation being driven by the molecular anisotropy.[25,31,33] Following these criteria, planar phosphorescent molecules with D_{nh} symmetry having cyclic conjugated π-systems, i.e., disk-shaped phosphors or fluorophores, are preferred. Polycyclic conjugated π-systems are sensitive to small changes of environment via large $\pi-\pi$ interactions.[24] Additionally, it is a simple matter for disk-shaped molecules to convert θ_{hor} to the average tilt angle of the molecular plane.[24] On the other hand, asymmetric planar molecules with one molecular axis larger than the other, i.e. with an aspect ratio >1, have distinct edges for a molecule to contact the substrate, causing difficulties distinguishing the high θ_{hor} either from a flat-lying or an edge-on configuration with the TDM axis parallel to the substrate plane. An example is dibenzo-(*f*,*h*)quinoxaline (Pt dipivaloylmethane)$_2$ in ref 27, which shows a horizontally aligned TDM with an edge-on configuration to the substrate. The complication becomes even more pronounced when the dye molecule has rotary σ-bonded aromatic chains that randomize the TDM orientation. Therefore, metal porphyrins or phthalocyanines are optimal sensing molecules for unambiguous orientation assignment.

In FIM, the majority of emission toward the substrate is collected by the objective lens. Also, the intensity profile of the entire *k*-space is simultaneously acquired in a single snapshot, enabling a dramatically reduced time for measurement compared to conventional, 1D angle scanning methods.[8] Consequently, it is possible to observe the emission from

https://dx.doi.org/10.1021/acs.nanolett.0c03440
Nano Lett. 2020, 20, 8290−8297

minute dye molecule concentrations. Indeed, submonolayer coverage by sensor molecules enables their precise placement at well-defined depths within the host as in Figure 3, enabling Ångstrom-level depth resolution that is limited only by the flatness of the predeposited film and the ability to accurately determine layer thickness during deposition. This is compared with commonly used morphological measurements such as atomic force microscopy (AFM), ellipsometry, and X-ray or electron beam diffractometry, that are only capable of revealing either surface structure or averaged information of the bulk. Electron tomography is another means for investigating the bulk morphology of the film. However, it requires crystalline film structures and atoms with high contrast (e.g., metals) to resolve the orientation or the arrangement of the molecules. Moreover, the high energy electron beam inflicts damage to the sample, especially for soft materials as organics. The position-selective character of the MSL enables investigating the interface morphology at planar heterojunctions or within donor−acceptor domains in mixed heterojunctions, which can be helpful in optimizing organic electronic device performance.[34] An example of an interface morphology measurement is sample P3 in Figure 3, determined by locating a submonolayer sensor layer between the CBP and TPBi layers. The horizontal alignment of the as-grown P3 sample shows that the initially deposited CBP molecules at the interface follow the morphology of the underlying layer (TPBi). However, the orientation in P4 is identical to the bulk CBP, demonstrating that effects of the underlying layer are not preserved as the deposition continues. At the air−CBP interface (P5), the orientation becomes increasingly vertical compared to P4, showing that surface crystallization of CBP is encouraged as its degrees of freedom increase with distance from the pinning interface. The change of $\theta_{\text{h-conv}}$ in P3 after annealing is smaller than P4−P5, which is still less than in Figure 2, region C. This suggests that depositing CBP on a stable layer suppresses morphological changes throughout the bulk of the film. This is similar to the structural forcing induced by molecular alignment to an underlying template layer.[33,35]

Ellipsometry has been commonly used for investigating the structure of buffer layers via analysis of the difference between ordinary and extraordinary refractive indices[36] as shown in Figure S4. The refractive index of a 30 nm thick triindolotriazine (Tint) film in Figure S4 demonstrates vertically aligned molecules, consistent with the result from XRD and FIM+MSL, showing that FIM+MSL could be extended into various organic materials. However, the birefringence of the film does not always reveal the actual molecular configuration since it solely probes the polarizability and the transition dipole moment of the film. For example, TPBi shows nearly isotropic orientation by ellipometry,[37] whereas the result for P2 in Figure 3, and the previous report from Mayr et al.[25] indicates the molecules have a preferred horizontal alignment. This difference arises from the molecular structure of TPBi (Figure 3a, inset) comprising three rotary σ-bonded aromatic chains that are randomized in the solid, resulting in suppressed birefringence for molecules that are horizontally aligned.

4. CONCLUSIONS

We spatially resolve the 3D morphology within organic electronic thin films by measuring the orientation of an ultrathin, luminescent morphological sensing layer using Fourier plane imaging microscopy. The MSL is deposited at the position of interest in a submonolayer quantity that has a minimal influence on the morphology of the film under study. The sensing molecules with discotic molecular structures are optimal for precisely representing the local structure. With this method, we measured the morphology at multiple depth positions within a planar heterojunction bilayer comprising films with different T_g, showing different morphological evolutions across the bilayer bulk with annealing. In addition, we investigated the morphology of the annealed film in various in-plane positions with micrometer scale features using a high-magnification objective lens in the FIM. The resolution of our morphology measurements is at the Ångstrom scale in the direction normal to the film plane and is optically diffraction limited within the plane.

Finally, although our measurements have been confined to the study of organic electronic thin film materials, we note that the technique can be applied in other vdW bonded solids such as two-dimensional semiconductors, quantum dots, and perovskites and, with appropriate modifications, to covalent and ionically bonded materials. Furthermore, depositing the MSL between different spin-coated films is also possible for analyzing solution processed materials.

■ ASSOCIATED CONTENT

Supporting Information

The Supporting Information is available free of charge at https://pubs.acs.org/doi/10.1021/acs.nanolett.0c03440.

Detailed explanation of the polar plot obtained from Fourier plane imaging microscopy, θ_{hor} conversion of PtOEP, dendritic growth of CBP on TPBi with annealing, morphological investigation of the Tint film via PtOEP MSL, refractive index of CBP film, and surface roughness and fitting error analysis (PDF)

■ AUTHOR INFORMATION

Corresponding Author

Stephen R. Forrest − *Department of Electrical & Computer Engineering, Department of Physics, and Department of Materials Science & Engineering, University of Michigan, Ann Arbor, Michigan 48109, United States;* orcid.org/0000-0003-0131-1903; Email: stevefor@umich.edu

Authors

Jongchan Kim − *Department of Electrical & Computer Engineering, University of Michigan, Ann Arbor, Michigan 48109, United States*

Shaocong Hou − *Department of Electrical & Computer Engineering, University of Michigan, Ann Arbor, Michigan 48109, United States*

Haonan Zhao − *Department of Physics, University of Michigan, Ann Arbor, Michigan 48109, United States*

Complete contact information is available at: https://pubs.acs.org/10.1021/acs.nanolett.0c03440

Author Contributions

J.K. designed the experiments, fabricated all samples, performed all measurements, constructed the simulation code for data fitting and analysis and analyzed the XRD data. S.C. assisted in designing the experiments and constructed the FIM measurement set up. H. Z. extended the simulation for anisotropic media. S.R.F. supervised the project, helped in

https://dx.doi.org/10.1021/acs.nanolett.0c03440
Nano Lett. 2020, 20, 8290−8297

experimental design, and analyzed the data. J.K. and S.R.F. wrote the manuscript together.

Notes

The authors declare the following competing financial interest(s): One of the authors of this paper (S.R.F.) has a minor equity interest in one of the sponsors (UDC, Inc.). This apparent conflict is under management by the University of Michigan Office of Research.

■ ACKNOWLEDGMENTS

The work was supported by the U.S. Department of Energy, Office of Basic Energy Sciences, Award DE-SC0017971 (experiment, analysis), and Universal Display Corporation (device applications).

■ REFERENCES

(1) Yang, F.; Shtein, M.; Forrest, S. R. Controlled Growth of a Molecular Bulk Heterojunction Photovoltaic Cell. *Nat. Mater.* **2004**, *4* (1), 37−41.
(2) Yokoyama, D. Molecular Orientation in Small-Molecule Organic Light-Emitting Diodes. *J. Mater. Chem.* **2011**, *21* (48), 19187−19202.
(3) Guerrero, A.; Garcia-Belmonte, G. Recent Advances to Understand Morphology Stability of Organic Photovoltaics. *Nano-Micro Lett.* **2017**, *9* (1), 10.
(4) Kim, C.; Facchetti, A.; Marks, T. J. Polymer Gate Dielectric Surface Viscoelasticity Modulates Pentacene Transistor Performance. *Science* **2007**, *318* (5847), 76−80.
(5) Savikhin, V.; Jagadamma, L. K.; Purvis, L. J.; Robertson, I.; Oosterhout, S. D.; Douglas, C. J.; Samuel, I. D. W.; Toney, M. F. Morphological, Chemical, and Electronic Changes of the Conjugated Polymer PTB7 with Thermal Annealing. *iScience* **2018**, *2*, 182−192.
(6) Sirringhaus, H.; Brown, P. J.; Friend, R. H.; Nielsen, M. M.; Bechgaard, K.; Langeveld-Voss, B. M. W.; Spiering, A. J. H.; Janssen, R. a. J.; Meijer, E. W.; Herwig, P.; de Leeuw, D. M. Two-Dimensional Charge Transport in Self-Organized, High-Mobility Conjugated Polymers. *Nature* **1999**, *401* (6754), 685−688.
(7) Lin, H.-W.; Lin, C.-L.; Chang, H.-H.; Lin, Y.-T.; Wu, C.-C.; Chen, Y.-M.; Chen, R.-T.; Chien, Y.-Y.; Wong, K.-T. Anisotropic Optical Properties and Molecular Orientation in Vacuum-Deposited Ter(9,9-Diarylfluorene)s Thin Films Using Spectroscopic Ellipsometry. *J. Appl. Phys.* **2004**, *95* (3), 881−886.
(8) Frischeisen, J.; Yokoyama, D.; Adachi, C.; Brütting, W. Determination of Molecular Dipole Orientation in Doped Fluorescent Organic Thin Films by Photoluminescence Measurements. *Appl. Phys. Lett.* **2010**, *96* (7), 073302.
(9) Ding, K.; Liu, X.; Forrest, S. R. Charge Transfer and Collection in Dilute Organic Donor−Acceptor Heterojunction Blends. *Nano Lett.* **2018**, *18* (5), 3180−3184.
(10) Chen, W.; Nikiforov, M. P.; Darling, S. B. Morphology Characterization in Organic and Hybrid Solar Cells. *Energy Environ. Sci.* **2012**, *5* (8), 8045−8074.
(11) Rohlfing, M.; Temirov, R.; Tautz, F. S. Adsorption Structure and Scanning Tunneling Data of a Prototype Organic-Inorganic Interface: PTCDA on Ag(111). *Phys. Rev. B: Condens. Matter Mater. Phys.* **2007**, *76* (11), 115421.
(12) Leijten, Z. J. W. A.; Keizer, A. D. A.; de With, G.; Friedrich, H. Quantitative Analysis of Electron Beam Damage in Organic Thin Films. *J. Phys. Chem. C* **2017**, *121* (19), 10552−10561.
(13) Lieb, M. A.; Zavislan, J. M.; Novotny, L. Single-Molecule Orientations Determined by Direct Emission Pattern Imaging. *J. Opt. Soc. Am. B* **2004**, *21* (6), 1210−1215.
(14) Schuller, J. A.; Karaveli, S.; Schiros, T.; He, K.; Yang, S.; Kymissis, I.; Shan, J.; Zia, R. Orientation of Luminescent Excitons in Layered Nanomaterials. *Nat. Nanotechnol.* **2013**, *8* (4), 271−276.
(15) Böhmler, M.; Hartmann, N.; Georgi, C.; Hennrich, F.; Green, A. A.; Hersam, M. C.; Hartschuh, A. Enhancing and Redirecting Carbon Nanotube Photoluminescence by an Optical Antenna. *Opt. Express* **2010**, *18* (16), 16443.
(16) Brown, S. J.; DeCrescent, R. A.; Nakazono, D. M.; Willenson, S. H.; Ran, N. A.; Liu, X.; Bazan, G. C.; Nguyen, T.-Q.; Schuller, J. A. Enhancing Organic Semiconductor−Surface Plasmon Polariton Coupling with Molecular Orientation. *Nano Lett.* **2017**, *17* (10), 6151−6156.
(17) Fieramosca, A.; De Marco, L.; Passoni, M.; Polimeno, L.; Rizzo, A.; Rosa, B. L. T.; Cruciani, G.; Dominici, L.; De Giorgi, M.; Gigli, G.; Andreani, L. C.; Gerace, D.; Ballarini, D.; Sanvitto, D. Tunable Out-of-Plane Excitons in 2D Single-Crystal Perovskites. *ACS Photonics* **2018**, *5* (10), 4179−4185.
(18) Gao, Y.; Weidman, M. C.; Tisdale, W. A. CdSe Nanoplatelet Films with Controlled Orientation of Their Transition Dipole Moment. *Nano Lett.* **2017**, *17* (6), 3837−3843.
(19) Jurow, M. J.; Morgenstern, T.; Eisler, C.; Kang, J.; Penzo, E.; Do, M.; Engelmayer, M.; Osowiecki, W. T.; Bekenstein, Y.; Tassone, C.; Wang, L.-W.; Alivisatos, A. P.; Brütting, W.; Liu, Y. Manipulating the Transition Dipole Moment of $CsPbBr_3$ Perovskite Nanocrystals for Superior Optical Properties. *Nano Lett.* **2019**, *19* (4), 2489−2496.
(20) Pommier, D.; Bretel, R.; López, L. E. P.; Fabre, F.; Mayne, A.; Boer-Duchemin, E.; Dujardin, G.; Schull, G.; Berciaud, S.; Le Moal, E. Scanning Tunneling Microscope-Induced Excitonic Luminescence of a Two-Dimensional Semiconductor. *Phys. Rev. Lett.* **2019**, *123* (2), 027402.
(21) Taminiau, T. H.; Stefani, F. D.; Segerink, F. B.; van Hulst, N. F. Optical Antennas Direct Single-Molecule Emission. *Nat. Photonics* **2008**, *2* (4), 234−237.
(22) Taminiau, T. H.; Karaveli, S.; van Hulst, N. F.; Zia, R. Quantifying the Magnetic Nature of Light Emission. *Nat. Commun.* **2012**, *3* (1), 979.
(23) Kim, J.; Zhao, H.; Hou, S.; Khatoniar, M.; Menon, V.; Forrest, S. R. Using Fourier-Plane Imaging Microscopy for Determining Transition-Dipole-Moment Orientations in Organic Light-Emitting Devices. *Phys. Rev. Appl.* **2020**, *14* (3), 034048.
(24) Huh, J.-S.; Kim, K.-H.; Moon, C.-K.; Kim, J.-J. Dependence of Pt(II) Based Phosphorescent Emitter Orientation on Host Molecule Orientation in Doped Organic Thin Films. *Org. Electron.* **2017**, *45*, 279−284.
(25) Mayr, C.; Brütting, W. Control of Molecular Dye Orientation in Organic Luminescent Films by the Glass Transition Temperature of the Host Material. *Chem. Mater.* **2015**, *27* (8), 2759−2762.
(26) Low, P. J.; Paterson, M. A. J.; Yufit, D. S.; Howard, J. A. K.; Cherryman, J. C.; Tackley, D. R.; Brook, R.; Brown, B. Towards an Understanding of Structure−Property Relationships in Hole-Transport Materials: The Influence of Molecular Conformation on Oxidation Potential in Poly(Aryl)Amines. *J. Mater. Chem.* **2005**, *15* (23), 2304−2315.
(27) Peumans, P.; Bulović, V.; Forrest, S. R. Efficient Photon Harvesting at High Optical Intensities in Ultrathin Organic Double-Heterostructure Photovoltaic Diodes. *Appl. Phys. Lett.* **2000**, *76* (19), 2650−2652.
(28) Peumans, P.; Uchida, S.; Forrest, S. R. Efficient Bulk Heterojunction Photovoltaic Cells Using Small-Molecular-Weight Organic Thin Films. *Nature* **2003**, *425* (6954), 158−162.
(29) Magill, J. H. Review Spherulites: A Personal Perspective. *J. Mater. Sci.* **2001**, *36* (13), 3143−3164.
(30) Huh, J.-S.; Kim, K.-H.; Kim, J.-J. Emitting Dipole Orientation and Molecular Orientation of Homoleptic Ir(III) Complexes. *Org. Electron.* **2020**, *82*, 105715.
(31) Jurow, M. J.; Mayr, C.; Schmidt, T. D.; Lampe, T.; Djurovich, P. I.; Brütting, W.; Thompson, M. E. Understanding and Predicting the Orientation of Heteroleptic Phosphors in Organic Light-Emitting Materials. *Nat. Mater.* **2016**, *15* (1), 85−91.
(32) Lin, H.-W.; Lin, C.-L.; Wu, C.-C.; Chao, T.-C.; Wong, K.-T. Influences of Molecular Orientations on Stimulated Emission Characteristics of Oligofluorene Films. *Org. Electron.* **2007**, *8* (2−3), 189−197.

https://dx.doi.org/10.1021/acs.nanolett.0c03440
Nano Lett. 2020, 20, 8290−8297

(33) Kim, J.; Batagoda, T.; Lee, J.; Sylvinson, D.; Ding, K.; Saris, P. J. G.; Kaipa, U.; Oswald, I. W. H.; Omary, M. A.; Thompson, M. E.; Forrest, S. R. Systematic Control of the Orientation of Organic Phosphorescent Pt Complexes in Thin Films for Increased Optical Outcoupling. *Adv. Mater.* **2019**, *31* (32), 1900921.
(34) Cheng, X.; Noh, Y.-Y.; Wang, J.; Tello, M.; Frisch, J.; Blum, R.-P.; Vollmer, A.; Rabe, J. P.; Koch, N.; Sirringhaus, H. Controlling Electron and Hole Charge Injection in Ambipolar Organic Field-Effect Transistors by Self-Assembled Monolayers. *Adv. Funct. Mater.* **2009**, *19* (15), 2407−2415.
(35) Fenter, P.; Schreiber, F.; Zhou, L.; Eisenberger, P.; Forrest, S. R. *In Situ* Studies of Morphology, Strain, and Growth Modes of a Molecular Organic Thin Film. *Phys. Rev. B: Condens. Matter Mater. Phys.* **1997**, *56* (6), 3046−3053.
(36) Yokoyama, D.; Sakaguchi, A.; Suzuki, M.; Adachi, C. Horizontal Orientation of Linear-Shaped Organic Molecules Having Bulky Substituents in Neat and Doped Vacuum-Deposited Amorphous Films. *Org. Electron.* **2009**, *10* (1), 127−137.
(37) Watanabe, Y.; Sasabe, H.; Yokoyama, D.; Beppu, T.; Katagiri, H.; Pu, Y.-J.; Kido, J. Simultaneous Manipulation of Intramolecular and Intermolecular Hydrogen Bonds in N-Type Organic Semiconductor Layers: Realization of Horizontal Orientation in OLEDs. *Adv. Opt. Mater.* **2015**, *3* (6), 769−773.

https://dx.doi.org/10.1021/acs.nanolett.0c03440
Nano Lett. 2020, 20, 8290−8297